

Flow Estimation Only from Image Data, based on Persistent Homology

Anna Suzuki (✉ anna.suzuki@tohoku.ac.jp)

Tohoku University

Miyuki Miyazawa

Tohoku University

James Minto

University of Strathclyde

Takeshi Tsuji

Kyushu University

Ippei Obayashi

RIKEN

Yasuaki Hiraoka

Kyoto University

Takatoshi Ito

Tohoku University

Research Article

Keywords: topological data analysis, persistent homology, physical properties, flow channels, fracture networks

Posted Date: March 29th, 2021

DOI: <https://doi.org/10.21203/rs.3.rs-330050/v1>

License:  This work is licensed under a Creative Commons Attribution 4.0 International License.

[Read Full License](#)

Flow Estimation Only from Image Data, based on Persistent Homology

Anna Suzuki^{1*}, Miyuki Miyazawa¹, James Minto², Takeshi Tsuji^{3,4}, Ippei Obayashi⁵,
Yasuaki Hiraoka⁶, and Takatoshi Ito¹

¹ Institute of Fluid Science, Tohoku University, Sendai 980-8577, Japan

² Department of Civil & Environmental Engineering, University of Strathclyde, Glasgow, UK

³ Department of Earth Resources Engineering, Kyushu University, Fukuoka 819-0385, Japan

⁴ International Institute for Carbon Neutral Energy Research (WPI-I2CNER), Kyushu University,
Fukuoka 819-0385, Japan

⁵ Center for Advanced Intelligence Project, RIKEN, Tokyo 103-0027, Japan

⁶ Kyoto University Institute for Advanced Study, ASHBI, Kyoto University, Kyoto 606-8501, Japan

*corresponding author(s): Anna Suzuki (anna.suzuki@tohoku.ac.jp)

Abstract (147 words)

Topological data analysis is an emerging concept of data analysis for characterizing shapes. A state-of-the-art tool in topological data analysis is persistent homology, which is expected to summarize quantified topological and geometric features. Although persistent homology is useful for revealing the topological and geometric information, it is difficult to interpret the parameters of persistent homology themselves and difficult to directly relate the parameters to physical properties. In this study, we focus on connectivity and apertures of flow channels detected from persistent homology analysis. We propose a method to estimate permeability in fracture networks from parameters of persistent homology. Synthetic 3D fracture network patterns and their direct flow simulations are used for the validation. The results suggest that the persistent homology can estimate fluid flow in fracture network based on the image data. This method can easily derive the flow phenomena based on the information of the structure.

Introduction

Fluid flow processes are ubiquitous in the world, and most are governed by the geometry and nature of the surrounding structures. In particular, recent miniaturization of artificial devices has led to the need for understanding and controlling flow in finer structures. It is also attracting attention to understand flow behaviors in complex fracture networks in developments of natural resources, as in the case of shale gas and geothermal developments.

It has been a long-term scientific challenge to predict flow behavior of porous media from structural properties. Permeability is a key parameter for examining flow phenomena in porous media¹. Permeability cannot be determined only from structure data, and needs to be obtained from laboratory experiments or numerical fluid flow simulations. In contrast, porosity is a parameter that is often used to characterize the structures. The porosity-permeability correlation has been studied extensively in the literature to estimate permeability using porosity (so-called Kozeny-Carman equation)^{2,3}. This Kozeny-Carman equation provides a relationship between structure and flow. The correlation has been studied extensively in the literature to estimate permeability using porosity. However, no matter how much void there are, if they are not connected, water cannot flow. Therefore, the Kozeny-Carman equation does not always work. The correlation has been modified to represent real phenomena by adding parameters such as fractal dimension, and tortuosity². These additional parameters can only be determined by fitting, which is not the best way to go about flow prediction based on structural information.

Let us also consider flow in a channel from an inlet to an outlet. Hagen-Poiseuille equation is a physical law that describe a steady laminar flow of a viscous, incompressible, and Newtonian fluid through a circular tube of constant radius, r . This is an exact solution for the

51 flow, can be derived from the (Navier-) Stokes equations, and is another way of expressing the
52 relationship between structure and flow. Using Darcy’s law, a representative permeability, K_{HP}
53 [m²], for the capillary can be calculated depending only on the radius:

$$54 \quad K_{HP} = \frac{r^2}{8} \quad (1)$$

56
57
58 Similarly, for flow in a fracture bounded by two smooth, parallel walls, the permeability, K_{CL}
59 [m²], can be calculated depending only on the aperture, h [m]:

$$60 \quad K_{CL} = \frac{h^2}{12} \quad (2)$$

61
62
63 Since the flow rate is proportional to the cube of the fracture aperture, this relationship between
64 flow and aperture is well-known as the “cubic law”⁴⁻⁷.

65 Eqs. (1) and (2) are only ways to obtain simplified analytic solution to describe the
66 relationship between the flow and structures. This is another way to predict permeability from
67 structural properties⁸. In natural rocks, it is not always a single fracture, but multiple fractures
68 that form a network. Thus, it is necessary to understand not just an individual fracture, but how
69 channels are connected from an inlet to an outlet in whole networks. There have been many
70 studies focusing on networks, but most of the parameters used to describe the structure are
71 probabilistic variables that capture individual fractures, and no suitable parameters have been
72 found yet to evaluate the flow of the entire networks⁹.

73 Topology, a branch of modern mathematics, is good at roughly investigating the
74 connectivity of shapes. Topology focuses on the properties (called topological properties or
75 topological invariants) that are preserved when some form (shape or space) is continuously
76 deformed (stretched or bent, but not cut or pasted). Topology can extract global features that
77 are difficult to capture with machine learning and convolutional neural networks, so it is
78 promising as a complementary feature to extract image information that cannot be detected
79 with other methods. It can be applied to volumetric data as well, so it can pick up information
80 that has been missed in one-way slice-by-slice analysis common to many forms of data
81 processing.

82 Several studies used topological invariants to describe pore-scale structures in porous
83 materials and fracture networks^{10,11}. The Minkowski functionals can be interpreted as area,
84 perimeter, or the Euler characteristic, which is a topological constant and were used to link to
85 hydraulic properties^{12,13}. Scholz et al. (2012)¹⁴ showed an empirical expression of permeability
86 with the Minkowski functionals Liu et al. (2017)¹⁵ showed the correlation of relative
87 permeability to one of the topological invariants called Euler characteristic. Armstrong et al.
88 (2019)¹⁶ reviewed the theoretical basis of the Minkowski functionals and its application to
89 characterize porous media. Counting the number of holes using topological invariants like they
90 did is a clue to the shape of the object, and the "essential information" can be extracted well.
91 On the other hand, topology too narrowly focuses on the essential information, it also discards
92 a lot of information, such as size of pore space. The size information, such as radii of tube or
93 apertures of fractures in Eqs. (1) and (2), must be detected to determine permeability derived
94 analytically. Therefore, previous studies had to add the size information in other ways.

95 Homology is a standard technique for identifying a topological space. In particular, the
96 concept of homology has traditionally played a role in feature extraction focusing on the
97 existence of “holes”. Here, the “hole” structure can be regarded as a connected flow channels
98 from an inlet to an outlet. It is expected that topology can be used to detect such connected
99 flow channels.

100 By tracking the sequence of topological spaces, namely, by recording how long
101 homological features persist, we can add information about the size and length of the holes.
102 This can give us a quantitative indication of the size of the holes and the amount of space
103 available, which is called persistent homology. Persistent homology is one of the most
104 important tools in topological data analysis and is expected to compute geometric and
105 topological features of various shapes with ease of computation^{17–20}. Thus, this has been
106 applied in several research fields^{21–25}, and is also beginning to be used in the analysis of porous
107 materials^{26–31}.

108 At this point, in contrast to topological invariants, persistent homology can provide a
109 lot of information that we might need, but it is difficult to interpret the parameters of persistent
110 homology themselves^{27–30}. Ushizima et al. (2012)²⁶ estimates permeability of porous rocks by
111 using Reeb graphs to represent the pore networks. They use persistent homology to distinguish
112 between significant and “noisy” pore spaces, and to supplement the Reeb graphs. Their paper
113 did not go into quantitative evaluation, but focused on qualitative evaluation and visualization.
114 As mentioned before, the “hole” structure that is characterized by topology, can be regarded as
115 connected flow channels from an inlet to an outlet. The aim of our study is to detect the flow
116 channels by persistent homology. Suzuki et al. (2020)³¹ proposes a method to detect flow
117 channels in 2D images from persistent homology through image processing. By using their
118 image processing procedure, persistent homology is expected to detect such connected flow
119 channels in complex fracture networks and would also provide their size information such as
120 apertures to predict the permeability.

121 In this study, we applied persistent homology to estimate permeability in fracture
122 networks based on image data. Persistent homology was used to detect the number of flow
123 channels and their apertures in the networks. Synthetic fracture networks were generated, and
124 direct flow simulation was conducted. Permeability derived from persistent homology and
125 simulation results were compared. We applied the proposed method to several published image
126 data and discussed the applicability of permeability estimation based on persistent homology.
127

128 **Results**

129 **Detection of flow channels from persistent homology analysis**

130 An example of a fractured rock model with a flow channel connecting an inlet to an
131 outlet is shown in Figure 1a. The yellow area is a solid skeleton, while the white area is
132 fractures forming void spaces. The connecting fractures from the top (inlet) to the bottom
133 (outlet) can be a flow channel. In persistent homology analysis, such structure is recognized as
134 “hole” and quantified as a 1-dimensional hole. Additionally, a discrete island (i.e., connected
135 component) is quantified as a 0-dimensional hole, and a ball (i.e., enclosed solid voids) is
136 quantified as a 2-dimensional hole. The numbers of k -dimensional holes (the dimension of the
137 k th homology vector space) are known to the k th Betti number (β_0 , β_1 , and β_2). This study
138 focuses on “hole” structures penetrating from an inlet to an outlet, which can be flow channels
139 hence we only analyze 1-dimensional holes in this study.

140 One aspect of persistent homology analysis is that independent fractures are recognized
141 as 2-dimensional holes, as shown in Figure 1b. These independent fractures would not
142 contribute to the fluid flow. Therefore, we can distinguish fractures that act as flow channels
143 and independent fractures by 1-dimensional holes and 2-dimensional holes.
144

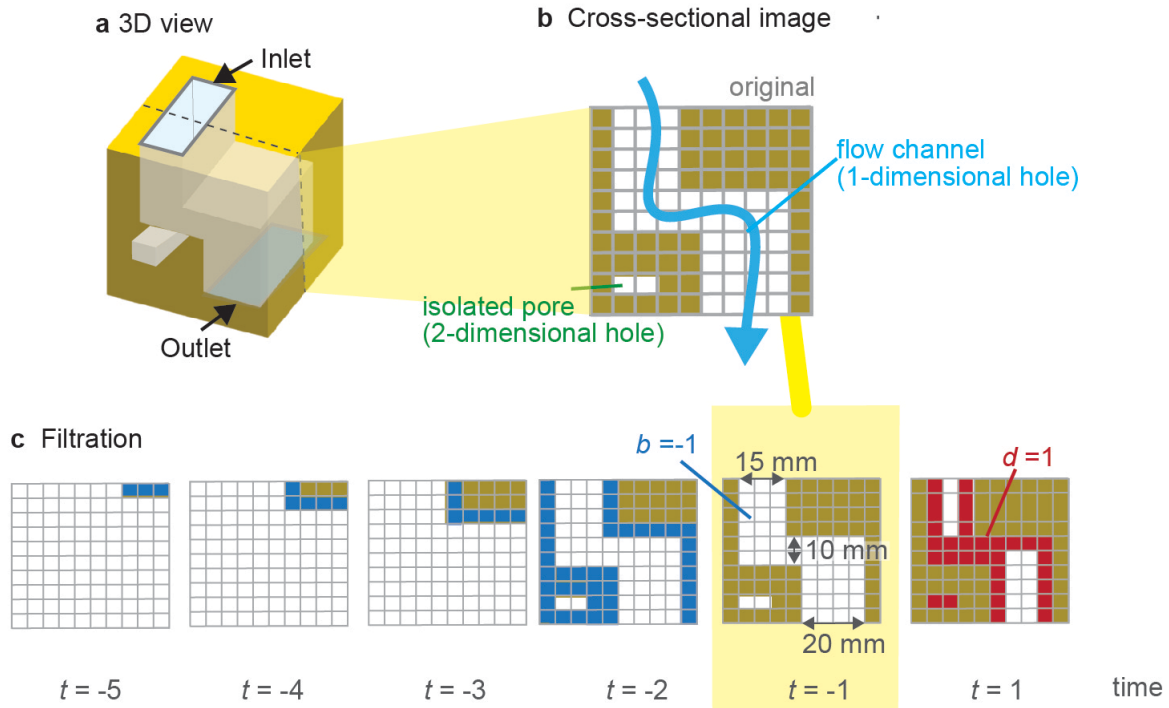


Figure 1 | Persistent homology analysis for fracture networks by HomCloud³². **a** 3D view and **b** cross-sectional image of fracture network with a flow channel (light blue arrow) and an isolated pore (mentioned as green). **c** Schematic of filtration process. Image at $t = -1$ is the original image. White grids express void spaces. Blue grids are the grids that were removed during the thinning process. Red grids are the grids that were added during the thickening process.

Much research has explored various applications of persistent homology in statistical data analysis of point cloud data^{22,33,34}. Since the purpose of this study is to analyze the information of structures based on the image data (e.g., micro-CT images), binarized digital images were used for analysis. Jiang et al. (2018)²⁹ applied persistent homology to analyzed rock pore geometries obtained from micro-CT images. The rock pore geometries were first represented as sphere cloud data using a pore-network extraction method, then analyzed by calculating the Vietoris-Rips complex topology of the input sphere cloud data. We used an open software HomCloud (<https://homcloud.dev/>) to analyze binarized 3D images, which can obtain the information of persistent homology by calculating the Euclidian distance of 2D or 3D black and white images³².

Figure 1c shows an example of data process in our persistent homology analysis, called filtration¹⁷. In filtration, the solid skeletons (yellow parts) are made thinner or thicker, voxel-by-voxel. The original image is set to -1 . The process of thinning yellow voxels adjacent to white voxels is regarded as -1 , while the process of thickening yellow voxels adjacent to white voxels is regarded as $+1$. When we reduce the time, the space eventually becomes empty. The nested sequence of the topological spaces from the empty space to the filled space is recorded. The times when the hole appears or disappears are called “birth time” or “death time”, expressed as “ b ” or “ d ”, respectively.

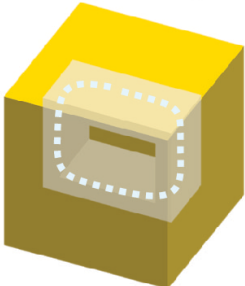
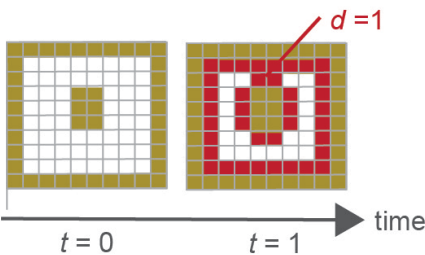
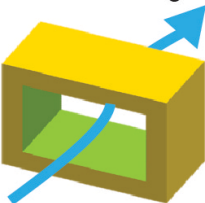
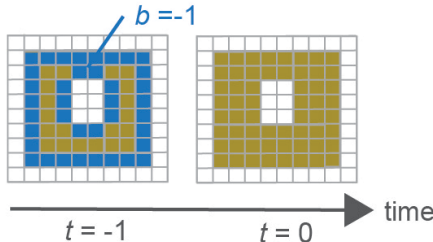
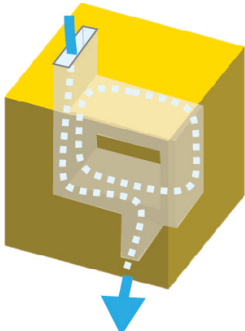
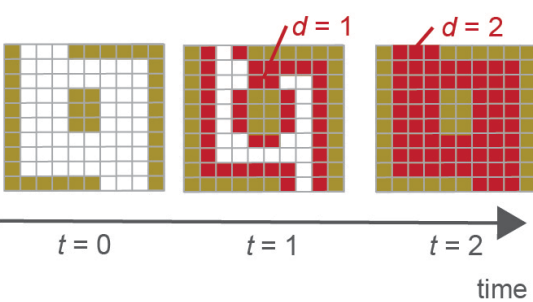
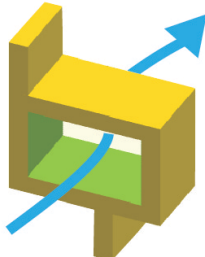
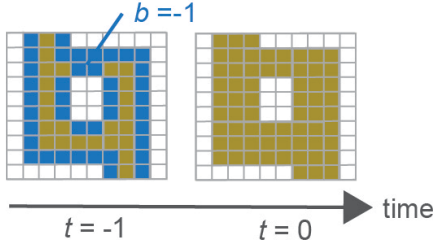
In filtration (Figure 1c), a point of the flow channel is closed at $t = 1$. This closed point is the narrowest aperture in the flow channel. Taking advantage of this, the length of narrowest aperture can be obtained as death time d multiplied by two and its resolution δ . (narrowest

174 aperture = $2 \times d \times \delta = 2 \times 1 \times 5 = 10$). It has been known that the narrowest width in flow
175 channels, which is called critical pore radius, correlates with permeability better than other pore
176 radii³⁵⁻³⁷. Detecting narrowest aperture by persistent homology can therefore be useful to
177 estimate the permeability.

178 The set of pairs (b_i, d_i) for k -dimensional holes is called k th persistence diagram, PD_k .
179 If pairs of negative b and positive d ($b < 0 < d$) are detected in PD_1 , the pairs suggest “hole”
180 structures (i.e., flow channel) presenting in the original image. If there are multiple hole
181 structures, multiple birth-death pairs are obtained in the $b < 0 < d$ domain of PD_1 . Each value
182 of d indicates each narrowest aperture of multiple fracture channels. The ability to link between
183 the numbers of flow channels and its narrowest apertures is one of the strengths of persistent
184 homology analysis.

185 Here is something to keep in mind. A 1-dimensional hole detected by persistent
186 homology is a flow channel penetrating from an inlet to an outlet. At the same time, a ring-
187 shaped, internal void-structures is also detected as a 1-dimensional hole. Figure 2a shows an
188 example of a ring-shaped internal void structure. This structure does not connect to the outside
189 (i.e., no flow channel). However, during filtration, the internal void space is closed at $t = 1$ (d
190 = 1). If images include such hole structures, it would overestimate the number of flow channels.
191 Now, let us prepare an inverted image that the yellow and white are reversed as shown in Figure
192 2b. In filtration, a ring appears at $t - 1$, and the ring width is detected by the value of b ($b = -1$).
193 Therefore, we can expect to detect only the hole fractures that act as flow channels by
194 subtracting the holes recognized in the inverted image from the holes recognized in the original
195 image. We set the number of 1-dimensional holes (i.e., Betti number) obtained from the
196 original and inverted figures to β_1 and $\bar{\beta}_1$, respectively. The number of flow channels can be
197 derived as $\beta_1 - \bar{\beta}_1 = 1 - 1 = 0$ as shown in Figure 2a and 2b.

198 Another example is shown in Figure 2c. This is a ring-shaped internal void structure
199 with two channels that are connected to the outside. In this case, there are two 1-dimensional
200 holes ($\beta_1 = 2$) with $d = 1$ and $d = 2$. Figure 2d is the inverted image of Figure 2c. There are a
201 1-dimensional holes ($\beta_1 = 1$) with $d = 1$. By subtracting the holes recognized in the inverted
202 image from the holes recognized in the original image, the number of flow channels can be
203 calculated as $\beta_1 - \bar{\beta}_1 = 2 - 1 = 1$. At the same time, persistent homology analysis provides
204 the narrowest aperture of the flow channel by $d = 2$. From these analyses, we estimate the
205 number of channels and their narrowest aperture by using the inverted image in this study.
206

image	filtration	Betti number
a original image 		$\beta_1=1$
b inverted image 		$\bar{\beta}_1=1$
c original image 		$\beta_1=2$
d inverted image 		$\bar{\beta}_1=1$

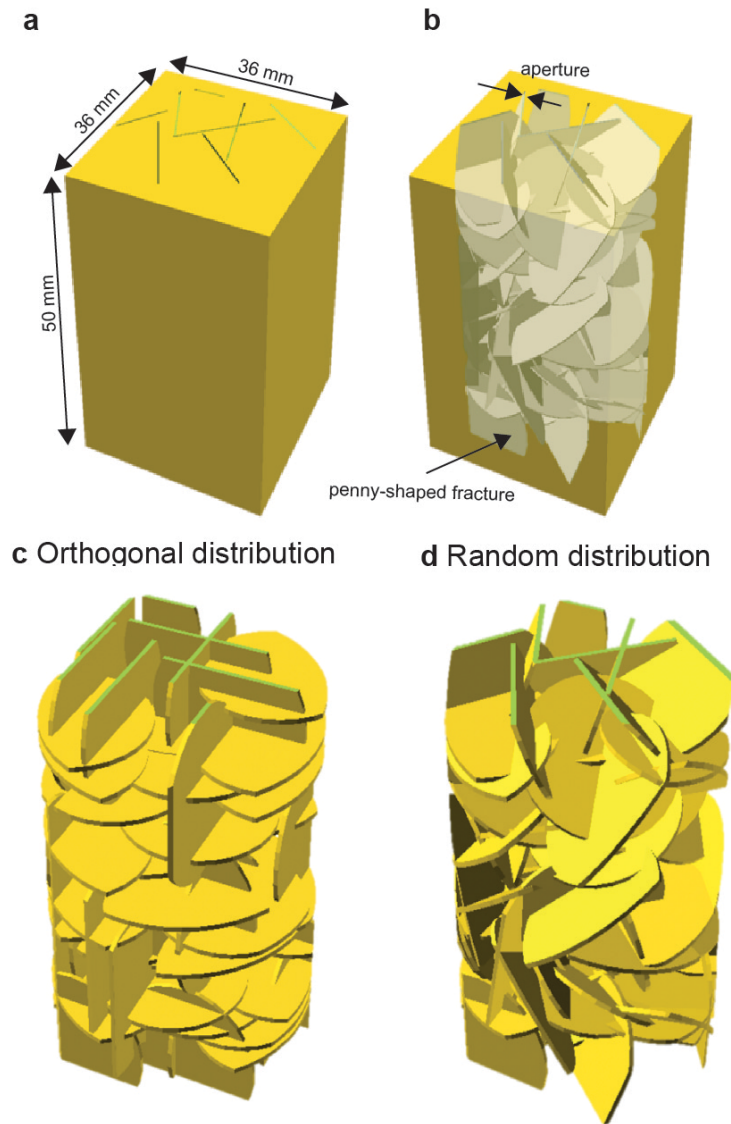
207
208
209
210
211
212
213
214

Figure 2 | Detecting flow channels using inverted images **a** ring-shaped, internal void-structure that is not connected to the outside, and **b** its inverted image. **c** ring-shaped, internal void-structure with two channels that is connected to the outside and forms a flow channel. **d** its inverted image. The left column shows 3D view of images. The center column describes processes of filtration. The right column lists Betti numbers β_1 .

215 **Synthetic fracture network**

216 Synthetic fracture networks were generated by using OpenSCAD
217 (<https://www.openscad.org/>). We distributed multiple penny-shaped fractures by controlling
218 the apertures, radii, numbers, and orientations of fractures to generate a fracture network³⁸. By
219 hollowing out the generated fracture network from a rectangular block, a fractured model
220 where the void spaces were composed of the fracture network was created. This study
221 characterizes one-dimensional flow. The top surface was an inlet, and the bottom surface was
222 an outlet. The fractures were connected from the top to the bottom surfaces. The side
223 boundaries were closed, and water did not flow out from the side.

224 The fractured model is shown in Figure 3. Figure 3a and 3b are the outside and the
225 inside of the model. The fracture orientation was either orthogonal or random. The orthogonal
226 models distributed perpendicular or horizontal fractures to the flow direction (Figure 3c), while
227 the random models distributed fractures by random numbers (Figure 3d). We prepared nine
228 orthogonal models and seven random models. The model parameters for each model are listed
229 in Table 1.



230 **Figure 3 | Fractured models.** a outside and b inside of model. c Orthogonal
231 distribution and d random distribution of fracture networks.
232
233

234
235

Table 1 | Fracture network parameters and results of permeability.

Model	Fracture network parameters				Simulation result	PH estimation
	Diameter (mm)	Aperture (mm)	Fracture density parameter	Number of fractures		
Orthogonal						
O1	10	0.2	3000	77	1.04×10^{-10}	2.47×10^{-10}
O2	10	0.6	3000	77	3.03×10^{-9}	3.43×10^{-9}
O3	10	1.0	3000	77	1.31×10^{-8}	1.55×10^{-8}
O4	5	0.2-1	6100	234	1.58×10^{-10}	2.68×10^{-10}
O5	10	0.2-1	1720	66	4.00×10^{-10}	7.18×10^{-10}
O6	5	0.2-1	2020	251	3.50×10^{-10}	2.70×10^{-10}
O7	5	0.2-1	13000	230	1.12×10^{-10}	2.16×10^{-10}
O8	5-25	0.2-1	895	73	3.15×10^{-9}	2.20×10^{-9}
Random						
R1	10	0.2	2000	77	1.01×10^{-10}	2.36×10^{-10}
R2	10	0.6	2000	77	2.90×10^{-9}	3.46×10^{-9}
R3	10	1.0	2000	77	1.28×10^{-8}	1.39×10^{-8}
R4	10	0.2	1000	38	3.42×10^{-11}	1.12×10^{-10}
R5	10	0.2	3000	115	1.75×10^{-10}	3.70×10^{-10}
R6	25	1.0	280	11	5.21×10^{-9}	4.03×10^{-9}
R7	5	0.2	11950	459	1.30×10^{-10}	1.36×10^{-10}

236

Estimation of fracture numbers and apertures by persistent homology

237

238

239

240

3D image data of each fractured model (36 mm × 36 mm × 50 mm with a voxel resolution δ of 0.1 mm) were binarized and analyzed by persistent homology using HomCloud³². The image size was 360 × 360 × 500 voxels.

241

242

243

244

245

246

247

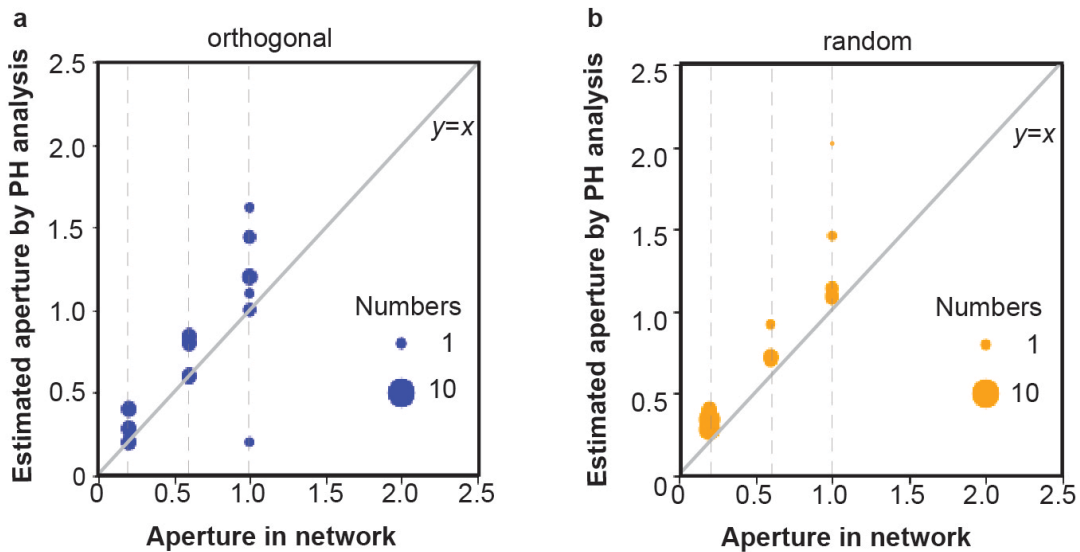
248

249

250

251

The estimated narrowest fracture apertures based on the persistent homology analysis are shown in Figure 4. Fracture networks (O1-O3, R1-R3) distributes a single value of fracture aperture of 0.2 mm, 0.6 mm, and 1.0 mm, respectively. Figures 4a and Figure 4b shows the results for the orthogonal and the random fracture networks, respectively. As mentioned before, the narrowest apertures in each flow channel were calculated as $2d_i \delta$ in persistent homology analysis. The values given in each network (0.2 mm, 0.6 mm, 1.0 mm) are compared with the estimated narrowest apertures ($2d_i \delta$). The sizes of the circles represent the number of birth-death pairs with d_i . As shown in Figure 4, the estimated narrowest apertures are equal or relatively larger than the actual values given in the network. Most of results are between one or two times larger than the actual values. Persistent homology analysis detects not fractures themselves but flow channels.



252

253

254

Figure 4 | Estimation of fracture apertures by persistent homology (PH) analysis. a orthogonal fracture networks and b random fracture networks.

255
 256
 257
 258
 259
 260
 261
 262
 263
 264
 265
 266
 267
 268
 269
 270
 271
 272
 273
 274
 275
 276
 277
 278
 279
 280
 281
 282
 283
 284
 285
 286
 287
 288
 289
 290
 291
 292
 293
 294
 295
 296
 297
 298
 299
 300

Derivation of permeability

We use Eq. (2) to derive permeability, which can be originally calculated by comparing the Stokes equation with the Darcy's law. If Assuming that a fracture is a smooth and parallel plate with the aperture of h and that there is a uniform pressure gradient in one direction within the plane of the fracture, the total volumetric flowrate in the fracture can be written as

$$Q_x = -\frac{wh^3}{12\mu} \frac{dP}{dx} \quad (3)$$

where w is the width of the fracture, perpendicular to the flow direction. h is the aperture, and μ is the water viscosity, dP/dx is the pressure gradient. Darcy's law describes one-dimensional fluid flow through porous media as

$$Q_x = -\frac{KA}{\mu} \frac{dP}{dx} \quad (4)$$

where A is the cross-sectional area. Comparison of Eqs. (3) and (4) shows that the permeability of the fracture can be identified as

$$K = -\frac{wh^3}{12A} \quad (5)$$

If the cross-sectional areas of the inlet and outlet are assumed to be wh , Eq. (5) becomes Eq. (2). If we consider the case of parallel multiple channels, the permeability can be derived in the following equation

$$K = \sum_{i=1}^N \frac{w_i h_i^3}{12A} \quad (6)$$

where A is the surface area of the cross section of the medium, and N is the number of flow channels. w_i is the depth of flow channel, and h_i is the aperture of the flow channel i , $i=1, \dots, N$. There is an unknown parameter w_i in Eq. (6). The 3D voxel data can be regarded as a series of 2D cross-sectional images. The 2D cross-sectional image data provides total area of pore space, A_p in each layer. If we introduce effective depth \bar{w} that is the same for all flow channels, \bar{w} can be derived by $\bar{w} = \frac{\min(A_p)}{\sum_{i=1}^N h_i}$ where $\min(A_p)$ is the minimum of total area of pore space for all layers. The number of flow channels N was estimated from the number of birth-death pairs, and the aperture h_i was estimated as $2d_i \delta$ in persistent homology analysis. Thus, Eq. (6) can be written as follows

$$K = \frac{\bar{w}}{12A} \sum_{i=1}^N (2d_i \delta)^3 \quad (7)$$

Estimation of permeability from persistent homology analysis

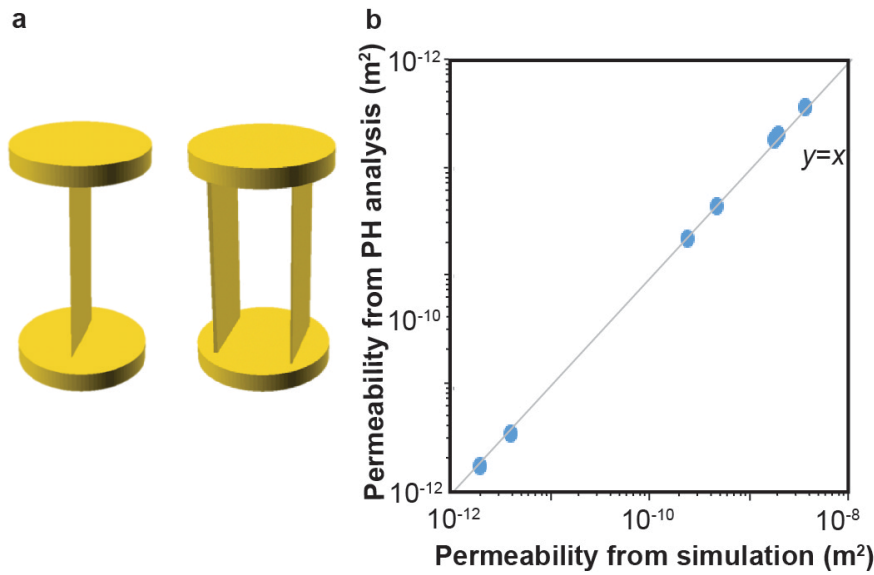
Before applying complex fracture networks, we validated Eq. (7) and our simulation with simple fracture models. Simple models with one or two fractures penetrating from an inlet to an outlet were used (see Figure 5a). Apertures and number of fractures in each model are listed in Table 2. Direct flow simulation with the same fracture network was conducted in OpenFOAM (<https://www.openfoam.com/>). We could obtain volumetric flow rate and pressure gradient between the inlet and the outlet to calculate equivalent permeability based on Darcy's law. Comparison of permeability between flow simulation and persistent homology analysis is shown in Figure 5b, and listed in Table 2. The persistent homology estimation is in

301 very good agreement with the simulation results. The results show that for such a simple system,
 302 persistent homology can estimate the permeability well using Eq. (7).

303
 304
 305

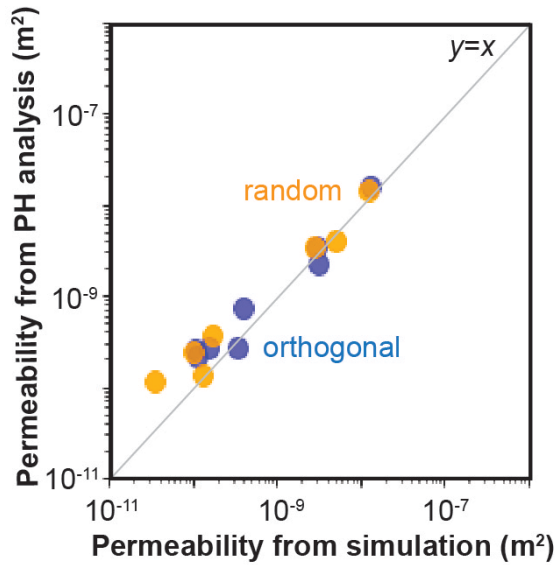
Table 2 | Estimation for simple parallel model.

Model	Aperture (mm)	Number of fractures	d	$\beta_1 - \overline{\beta_1}$	Simulation result	Estimation from PH analysis
S1	1.0	1	10	1	1.80×10^{-9}	1.80×10^{-9}
S2	1.0 and 1.0	2	10 and 10	2	3.66×10^{-9}	3.47×10^{-9}
S3	0.5	1	5	1	2.39×10^{-10}	2.17×10^{-10}
S4	0.5 and 0.5	2	5 and 5	2	4.79×10^{-10}	4.33×10^{-10}
S5	0.1	1	1	1	1.95×10^{-12}	1.73×10^{-12}
S6	0.1 and 0.1	2	1 and 1	2	3.89×10^{-12}	3.47×10^{-12}
S7	0.5 and 1.0	2	5 and 10	2	2.00×10^{-9}	1.95×10^{-9}



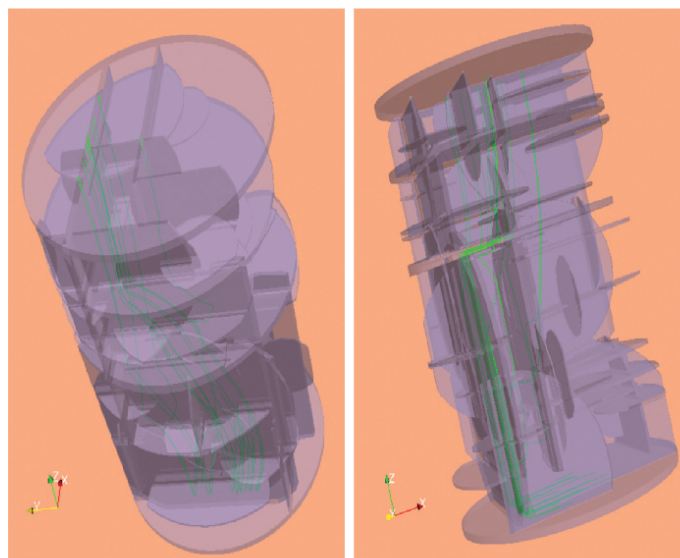
306 **Figure 5 | Validation with simple models.** **a** one or two fracture penetrating the
 307 model. The top and bottom are the inlet and the outlet. **b** Comparison of permeability
 308 between persistent homology (PH) analysis and direct simulation. The calculated
 309 permeability is listed in Table 2.
 310

311 Next, we applied Eq. (7) to complex fracture networks listed in Table 1. Comparison of
 312 permeability between flow simulation and persistent homology analysis is shown in Figure 6.
 313 The estimation is in reasonable agreement with the simulation results.



314
 315 **Figure 6 | Estimation of permeability by persistent homology (PH) analysis for**
 316 **orthogonal fracture networks (blue) and random fracture networks (orange).** The
 317 calculated permeability is listed in Table 1.

318
 319 There is a limitation of Eq. (7). Eq. (7) is based on a parallel plate model, so the flow
 320 is assumed to be straight. If there is tortuosity in a flow channel, the flow length will be longer,
 321 and the estimated permeability may be larger than the true value. Figure 7 shows streamlines
 322 in model O8 colored as green. We can see that the streamlines are winding and flowing. Keep
 323 in mind the fact that tortuosity was not taken into account in Eq. (7).

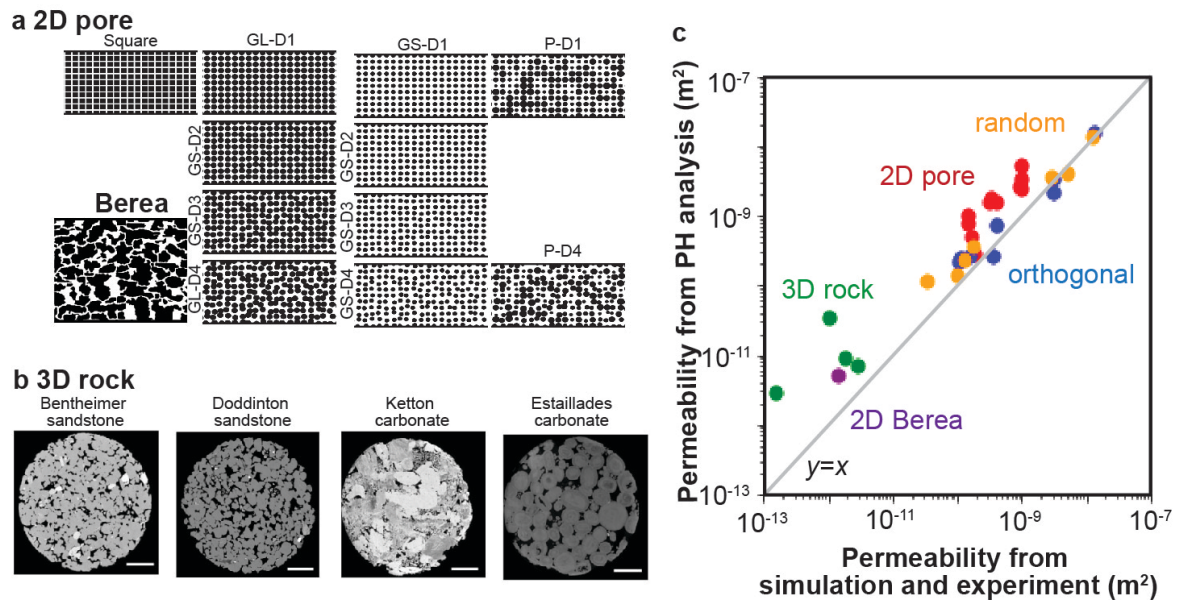


324
 325 **Figure 7 | Streamlines (green lines) in fracture network simulated in OpenFOAM.**

326
 327 We also applied persistent homology analysis to other cases. Mehmani and Mamdi
 328 (2015)³⁹ conducted high-fidelity direct numerical simulation of the two-dimensional
 329 micromodel to develop their pore network models. We used their 2D image data as shown in
 330 Figure 8a and their results from direct numerical simulation. Comparison with persistent
 331 homology analysis is plotted with red dots for regular pore structures and with purple dots for

332 Berea sandstone in Figure 8c. These results suggest that the proposed analysis can be used for
 333 two-dimensional flow.

334 Andrew et al. (2014)⁴⁰ used X-ray microtomography to obtain four types of 3D rock
 335 image data, and they conducted flow experiment to measure the permeability. The X-ray
 336 microtomography images of the rocks are shown in Figure 8b. Comparison with the
 337 experimental results is plotted as green dots in Figure 8c. Permeability estimated by persistent
 338 homology is larger than the experimental results. As mentioned before, Eq. (7) does not
 339 consider the effect of tortuosity. Muljadi et al. (2016)⁴¹ calculated the tortuosity from the same
 340 Bentheimer sandstone and the Estailades carbonate images as 1.52 and 1.91, respectively. If
 341 we take the tortuosity into account, the estimates of the permeability will be close to the
 342 experimental values. The calculation of tortuosity in Muljadi et al. (2016)⁴¹ used the flow
 343 velocity^{42,43}. In contrast, the goal of this study is to estimate flow properties without flow
 344 simulation, so that we need to obtain tortuosity in a different way based on image analysis.
 345 Correlation between tortuosity and persistent homology parameters would be explored in
 346 future studies.
 347



348 **Figure 8 | Estimation of permeability by persistent homology (PH) analysis.** **a** 2D
 349 images from Mehmani and Hamdi (2015)³⁹, **b** 3D rock images from Andrew et al.
 350 (2014)⁴⁰, and **c** comparison with direct simulation and experiment. The values are
 351 listed in Table 3.
 352

353
 354
 355
 356
 357
 358
 359
 360
 361
 362
 363
 364
 365

366
367

Table 3 | Information of 2D pore³⁹ and 3D rock images⁴⁰ and their permeability.

Model	Image size (pixels)	Domain size (mm)	Simulation result	PH estimation
2D pore				
Square			3.13×10^{-10}	1.54×10^{-9}
GL-D1			1.92×10^{-10}	2.74×10^{-10}
GL-D2			1.70×10^{-10}	4.96×10^{-10}
GL-D3			1.47×10^{-10}	7.98×10^{-10}
GL-D4			1.44×10^{-10}	9.71×10^{-10}
GS-D1	3000 x 1500	20 mm x 10 mm x 200 μm	9.77×10^{-10}	5.19×10^{-9}
GS-D2			9.75×10^{-10}	3.34×10^{-9}
GS-D3			9.60×10^{-10}	2.43×10^{-9}
GS-D4			9.18×10^{-10}	2.67×10^{-9}
P-D1			3.25×10^{-10}	1.75×10^{-9}
P-D4			4.01×10^{-10}	1.53×10^{-9}
Berea	2900 x 2320	1.774 mm x 1.418 mm x 24.54 μm	1.45×10^{-12}	5.06×10^{-12}
3D rock				
Model	Image size (voxels)	Resolution (um/px)	Experimental result	PH estimation
Doddington		2.6929	1.04×10^{-12}	3.37×10^{-11}
Bentheimer	300 x 300	3.0035	1.88×10^{-12}	9.02×10^{-11}
Ketton	x 300	3.00006	2.81×10^{-12}	6.86×10^{-11}
Estailades		3.31136	1.49×10^{-13}	2.90×10^{-11}

368
369

Discussions

370
371
372
373
374
375
376
377
378

Persistent homology analysis could estimate opening aperture distributions of flow channels and estimated permeability with the same order of magnitude as the permeability derived from the simulation. Using this method, flow characteristics can be estimated from the image data without the need for fluid flow simulation. This could make the analysis of fracture networks quicker. In this study, the longest direct flow simulation took 72 hours to generate a sufficiently high-resolution computational mesh then solve the Navier-Stokes equations, using 320 processors with a maximum of 282 GB of memory in a supercomputational system. In contrast, persistent homology was able to calculate the model in less than 10 minutes with 16 GB of memory using a desktop workstation AMD Ryzen 9 5950X.

379
380
381
382
383
384
385

Several approaches⁴⁴⁻⁴⁶ based on discrete fracture network represent fractures as ellipses or rectangles in networks based on Eq. (2). Focusing on the fractures themselves is suitable for fractured rock bodies, but it may be difficult to optimize the model because of the increase in number of parameters when the fractures are finer or when the body is regarded as a porous medium. In this study, we focus on the flow channels by persistent homology instead of individual fractures. Therefore, we can apply the method regardless of porous or fractured rocks.

386
387
388
389
390
391
392

Recently, some studies have been published to investigate the relationship between porous structures and flow by persistent homology^{29,30,47,48}. Most of them were machine learning approaches that put a large number of parameters into a black box. In contrast, since our approach focuses on flow-channel structures, permeability can be calculated by the simple and easy principle. We used the synthetic fracture networks as well as natural rocks. Although the estimation errors were relatively large for 3D rocks, it was shown that a simple model such as Eq. (7) can provide reasonably close estimates.

393
394
395

Ushizima et al. (2012)²⁶ estimates permeability of porous rocks by using Reeb graphs to represent the pore networks. They use persistent homology to distinguish between significant and noisy pore spaces, and to supplement the Reeb graphs. In fact, the Reeb graph

396 and persistent homology were used independently and separately. We think that using Reeb
397 graphs is a good direction to go to the next step.

398 We have succeeded in modeling physical phenomena from image data based on the
399 topological data analysis. The method could be applied also to a wide range of porous media
400 including artificial devices. It is expected to be applicable not only to estimate flow properties,
401 but also to characterize different transport phenomena, such as mass transfer, electrical and
402 magnetic flows.

403

404 Method

405 Persistent homology analysis

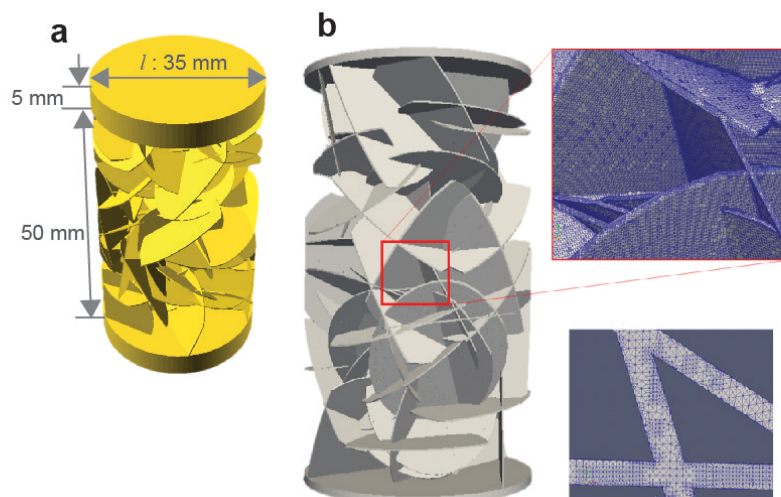
406 STL files of synthetic fracture networks were generated by using OpenSCAD, and the
407 STL files were converted to the cross-sectional images in 36 mm × 36 mm × 50 mm with a
408 voxel resolution of 0.1 mm in Autodesk Netfabb. To eliminate some unexpected noises, all the
409 images were blurred in XnConvert. The png files of the image data were analyzed in
410 HomCloud⁶³. When there were small differences between birth and death of PH₁, the hole
411 structure may appear during the image analysis. Thus, we neglected the result with $d_i - b_i < 2$
412 were eliminated.

413

414 Direct flow simulation

415 Flow behaviors in the rock models were simulated in OpenFOAM (ver. 4.1)³⁴, which
416 performs flow calculations based on the Navier-Stokes equation. The simulation used an STL
417 file of the network model, in which the upper and lower boundaries were added, as shown in
418 Figure 9a. Previous study validated the flow model with fracture networks similar to the rock
419 model in this study by creating test specimens from a 3D printer and conducting flow
420 experiment^{49,50}.

421 First, the meshes of the region were prepared (Figure 9b), and flow calculation of the
422 loaded STL file were performed using a steady-state turbulence solver for incompressible
423 fluids SIMPLE (Semi-Implicit Method for Pressure Linked Equations) method. In this study,
424 we set the flow rate to $1.75 \times 10^{-7} \text{ m}^3/\text{s}$, fluid viscosity to $9.32 \times 10^{-4} \text{ Pa}\cdot\text{s}$, and fluid density to
425 997.5 kg/m^3 .



426

427 **Figure 9 | Simulation in OpenFOAM.** a fracture network with upper and lower
428 boundaries. b discretized model.

429

430 Data availability

431 The data that support the findings of this study are available in
432 <https://figshare.com/s/cebf663b253d145bf8ac> (doi: 10.6084/m9.figshare.14110262, active
433 when the item is published), <https://figshare.com/s/de6df5d1cf76926c7f25> (doi:
434 10.6084/m9.figshare.14110208), <https://figshare.com/s/96f9d83791dc03e28ce0> (doi:
435 10.6084/m9.figshare.14113439).

436

437 Reference

- 438 1. Renard, P. & de Marsily, G. Calculating equivalent permeability: a review. *Adv.*
439 *Water Resour.* **20**, 253–278 (1997).
- 440 2. Costa, A. Permeability-porosity relationship: A reexamination of the Kozeny-
441 Carman equation based on a fractal pore-space geometry assumption.
442 *Geophys. Res. Lett.* **33**, 1–5 (2006).
- 443 3. Carman, P. C. Fluid flow through granular beds. *Trans. Chem. Eng.* **15**, S32–
444 S48 (1937).
- 445 4. Zimmerman, R. W. & Bodvarsson, G. S. Effective transmissivity of two-
446 dimensional fracture networks. *Int. J. Rock Mech. Min. Sci. Geomech. Abstr.*
447 **33**, 433–438 (1996).
- 448 5. Snow, D. Anisotropic Permeability of Fractured Media. *Water Resour. Res.* **5**,
449 1273–1289 (1969).
- 450 6. Renshaw, C. E. On the relationship between mechanical and hydraulic
451 apertures in rough-walled fractures. *J. Geophys. Res.* **100**, 629–636 (1995).
- 452 7. Witherspoon, P. A., Wang, J. S. Y., Iwai, K. & Gale, J. E. Validity of Cubic Law
453 for fluid flow in a deformable rock fracture. *Water Resour. Res.* **16**, 1016–1024
454 (1980).
- 455 8. Zimmerman, R. & Yeo, I. Fluid Flow in Rock Fractures: From the Navier-
456 Stokes Equations to the Cubic Law. *Dyn. fluids Fract. rock* 213–224 (2000).
457 doi:10.1029/GM122p0213
- 458 9. Hyman, J. D., Aldrich, G., Viswanathan, H., Makedonska, N. & Karra, S.
459 Fracture size and transmissivity correlations: Implications for transport
460 simulations in sparse three-dimensional discrete fracture networks following a
461 truncated power law distribution of fracture size. *Water Resour. Res.* **5**, 2–2
462 (1969).
- 463 10. Valentini, L., Perugini, D. & Poli, G. The “small-world” topology of rock fracture
464 networks. *Phys. A Stat. Mech. its Appl.* **377**, 323–328 (2007).
- 465 11. Andresen, C. A., Hansen, A., Le Goc, R., Davy, P. & Hope, S. M. Topology of
466 fracture networks. *Front. Phys.* **1**, 1–5 (2013).
- 467 12. Mecke, K. & Arns, C. H. Fluids in porous media: A morphometric approach. *J.*
468 *Phys. Condens. Matter* **17**, (2005).
- 469 13. Lehmann, P. *et al.* Impact of geometrical properties on permeability and fluid
470 phase distribution in porous media. *Adv. Water Resour.* **31**, 1188–1204 (2008).
- 471 14. Scholz, C. *et al.* Permeability of porous materials determined from the Euler
472 characteristic. *Phys. Rev. Lett.* **109**, 1–5 (2012).
- 473 15. Liu, Z., Herring, A., Arns, C., Berg, S. & Armstrong, R. T. Pore-Scale
474 Characterization of Two-Phase Flow Using Integral Geometry. *Transp. Porous*
475 *Media* **118**, 99–117 (2017).
- 476 16. Armstrong, R. T. *et al.* Porous Media Characterization Using Minkowski
477 Functionals: Theories, Applications and Future Directions. *Transp. Porous*
478 *Media* **130**, 305–335 (2019).
- 479 17. Edelsbrunner, H. & Harer, J. Persistent homology—a survey. *Contemp. Math.*
480 257–282 (2008). doi:10.1090/conm/453/08802

- 481 18. Zomorodian, A. & Carlsson, G. Computing persistent homology. *Proc. Annu.*
482 *Symp. Comput. Geom.* **274**, 347–356 (2004).
- 483 19. Edelsbrunner, H. & Morozov, D. Persistent Homology : Theory and Practice. in
484 *Conference: European Congress of Mathematics* (2012).
- 485 20. Weinberger, S. What is Persistent Homology? *Am. Math. Soc.* **58**, 36–39
486 (2010).
- 487 21. Chazal, F. & Michel, B. An introduction to topological data analysis:
488 Fundamental and practical aspects for data scientists. *arXiv* 1–38 (2017).
- 489 22. Otter, N., Porter, M. A., Tillmann, U., Grindrod, P. & Harrington, H. A. A
490 roadmap for the computation of persistent homology. *EPJ Data Sci.* **6**, (2017).
- 491 23. Kimura, M., Obayashi, I., Takeichi, Y., Murao, R. & Hiraoka, Y. Non-empirical
492 identification of trigger sites in heterogeneous processes using persistent
493 homology. *Sci. Rep.* **8**, 1–9 (2018).
- 494 24. Hiraoka, Y. *et al.* Hierarchical structures of amorphous solids characterized by
495 persistent homology. *Proc. Natl. Acad. Sci. U. S. A.* **113**, 7035–7040 (2016).
- 496 25. Ichinomiya, T., Obayashi, I. & Hiraoka, Y. Persistent homology analysis of
497 craze formation. *Phys. Rev. E* **95**, 1–6 (2017).
- 498 26. Ushizima, D. *et al.* Augmented topological descriptors of pore networks for
499 material science. *IEEE Trans. Vis. Comput. Graph.* **18**, 2041–2050 (2012).
- 500 27. Robins, V., Saadatfar, M., Delgado-Friedrichs, O. & Sheppard, A. P.
501 Percolating length scales from topological persistence analysis of micro-CT
502 images of porous materials. *Water Resour. Res.* **52**, 315–329 (2016).
- 503 28. Tsuji, T., Jiang, F., Suzuki, A. & Shirai, T. Mathematical Modeling of Rock Pore
504 Geometry and Mineralization: Applications of Persistent Homology and
505 Random Walk. 95–109 (2018). doi:10.1007/978-981-10-7811-8_11
- 506 29. Jiang, F., Tsuji, T. & Shirai, T. Pore Geometry Characterization by Persistent
507 Homology Theory. *Water Resour. Res.* **54**, 4150–4163 (2018).
- 508 30. Herring, A. L., Robins, V. & Sheppard, A. P. Topological Persistence for
509 Relating Microstructure and Capillary Fluid Trapping in Sandstones. *Water*
510 *Resour. Res.* **55**, 555–573 (2019).
- 511 31. Suzuki, A. *et al.* Inferring fracture forming processes by characterizing fracture
512 network patterns with persistent homology. *Comput. Geosci.* **143**, 104550
513 (2020).
- 514 32. Obayashi, I. & Hiraoka, Y. Persistence diagrams with linear machine learning
515 models. *arXiv* **1**, 421–449 (2017).
- 516 33. Choudhury, a. N. M. I., Wang, B., Rosen, P. & Pascucci, V. Topological
517 analysis and visualization of cyclical behavior in memory reference traces.
518 *2012 IEEE Pacific Vis. Symp.* 9–16 (2012).
519 doi:10.1109/PacificVis.2012.6183557
- 520 34. Choudhury, A. N. M. I., Wang, B., Rosen, P. & Pascucci, V. Topological
521 analysis and visualization of cyclical behavior in memory reference traces.
522 *IEEE Pacific Vis. Symp. 2012, PacificVis 2012 - Proc.* 9–16 (2012).
523 doi:10.1109/PacificVis.2012.6183557
- 524 35. Martys, N. & Garboczi, E. J. Length scales relating the quid permeability and
525 electrical conductivity in random two-dimensional model porous media. *Phys.*
526 *Rev. B* **46**, 6080–6090 (1992).
- 527 36. Schwartz, L. M., Martys, N., Bentz, D. P., Garboczi, E. J. & Torquato, S.
528 Cross-property relations and permeability estimation in model porous media.
529 *Phys. Rev. E* **48**, 4584–4591 (1993).
- 530 37. Nishiyama, N. & Yokoyama, T. Permeability of porous media: Role of the

- 531 critical pore size. *J. Geophys. Res. Solid Earth* **122**, 6955–6971 (2017).
532 38. Watanabe, K. & Takahashi, H. Fractal geometry characterization of
533 geothermal reservoir fracture networks. *Journal of Geophysical Research* **100**,
534 521–528 (1995).
535 39. Mehmani, Y. & Tchelepi, H. A. Minimum requirements for predictive pore-
536 network modeling of solute transport in micromodels. *Adv. Water Resour.* **108**,
537 83–98 (2017).
538 40. Andrew, M., Bijeljic, B. & Blunt, M. J. Pore-scale imaging of trapped
539 supercritical carbon dioxide in sandstones and carbonates. *Int. J. Greenh. Gas*
540 *Control* **22**, 1–14 (2014).
541 41. Muljadi, B. P., Blunt, M. J., Raeini, A. Q. & Bijeljic, B. The impact of porous
542 media heterogeneity on non-Darcy flow behaviour from pore-scale simulation.
543 *Adv. Water Resour.* **95**, 329–340 (2016).
544 42. Duda, A., Koza, Z. & Matyka, M. Hydraulic tortuosity in arbitrary porous media
545 flow. *Phys. Rev. E - Stat. Nonlinear, Soft Matter Phys.* **84**, 1–8 (2011).
546 43. Koponen, I. Analytic approach to the problem of convergence of truncated
547 Levy flights towards the Gaussian stochastic process. *Phys. Rev. E* **52**, 1197–
548 1199 (1995).
549 44. Jing, Y., Armstrong, R. T. & Mostaghimi, P. Image-based fracture pipe network
550 modelling for prediction of coal permeability. *Fuel* **270**, 117447 (2020).
551 45. Srinivasan, S., Karra, S., Hyman, J., Viswanathan, H. & Srinivasan, G. Model
552 reduction for fractured porous media: a machine learning approach for
553 identifying main flow pathways. *Comput. Geosci.* **23**, 617–629 (2019).
554 46. Srinivasan, G. *et al.* Quantifying Topological Uncertainty in Fractured Systems
555 using Graph Theory and Machine Learning. *Sci. Rep.* **8**, 1–11 (2018).
556 47. Robinson, J. *et al.* Imaging pathways in fractured rock using three-dimensional
557 electrical resistivity tomography. *Groundwater* **54**, 186–201 (2016).
558 48. Thakur, M. M., Kim, F., Penumadu, D. & Herring, A. Pore Space and Fluid
559 Phase Characterization in Round and Angular Partially Saturated Sands Using
560 Radiation-Based Tomography and Persistent Homology. *Transp. Porous*
561 *Media* (2021). doi:10.1007/s11242-021-01554-w
562 49. Suzuki, A., Watanabe, N., Li, K. & Horne, R. N. Fracture network created by 3-
563 D printer and its validation using CT images. *Water Resour. Res.* (2017).
564 doi:10.1002/2017WR021032
565 50. Suzuki, A., Minto, J. M., Watanabe, N., Li, K. & Horne, R. N. Contributions of
566 3D Printed Fracture Networks to Development of Flow and Transport Models.
567 *Transp. Porous Media* **129**, 485–500 (2019).
568

569 Acknowledgements

570 Anna Suzuki was supported by JSPS KAKENHI Grant Numbers JP20H02676 and
571 JP17H04976 (Japan); JST ACT-X Grant Number JPMJAX190H (Japan). Ippei Obayashi was
572 supported by JSPS KAKENHI Grant Number JP 16K17638, JP 19H00834, JP 20H05884;
573 JST PRESTO Grant Number JPMJPR1923; JST CREST Mathematics Grant number
574 15656429 (Japan); and the Structural Materials for Innovation, Strategic Innovation
575 Promotion Program D72 (Japan), which are gratefully acknowledged. The authors would like
576 to thank Department of Earth Science and Engineering, Imperial College London for sharing
577 the micro-CT data of the rocks. These micro-CT data can be downloaded through their web
578 page: [http://www.imperial.ac.uk/earth-sci-ence/research/research-groups/perm/
579 research/pore-scale-modelling/micro-ct-images-and-networks/](http://www.imperial.ac.uk/earth-sci-ence/research/research-groups/perm/research/pore-scale-modelling/micro-ct-images-and-networks/).
580

581 **Author contributions**

582 A.S. initiated the key concepts, designed, conducted persistent homology analysis, and
583 supervised the research. M.M. performed numerical simulation and conducted persistent
584 homology analysis. J.M. assisted flow simulation. I.O. and Y.H. assisted persistent homology
585 analysis. T.T and T.I conducted project administration. A.S. wrote the original draft. J.M.,
586 I.O., Y.H., T.T and T.I reviewed and edited the manuscript.

587

588 **Conflicts of Interest**

589 The authors declare no conflict of interest.

Figures

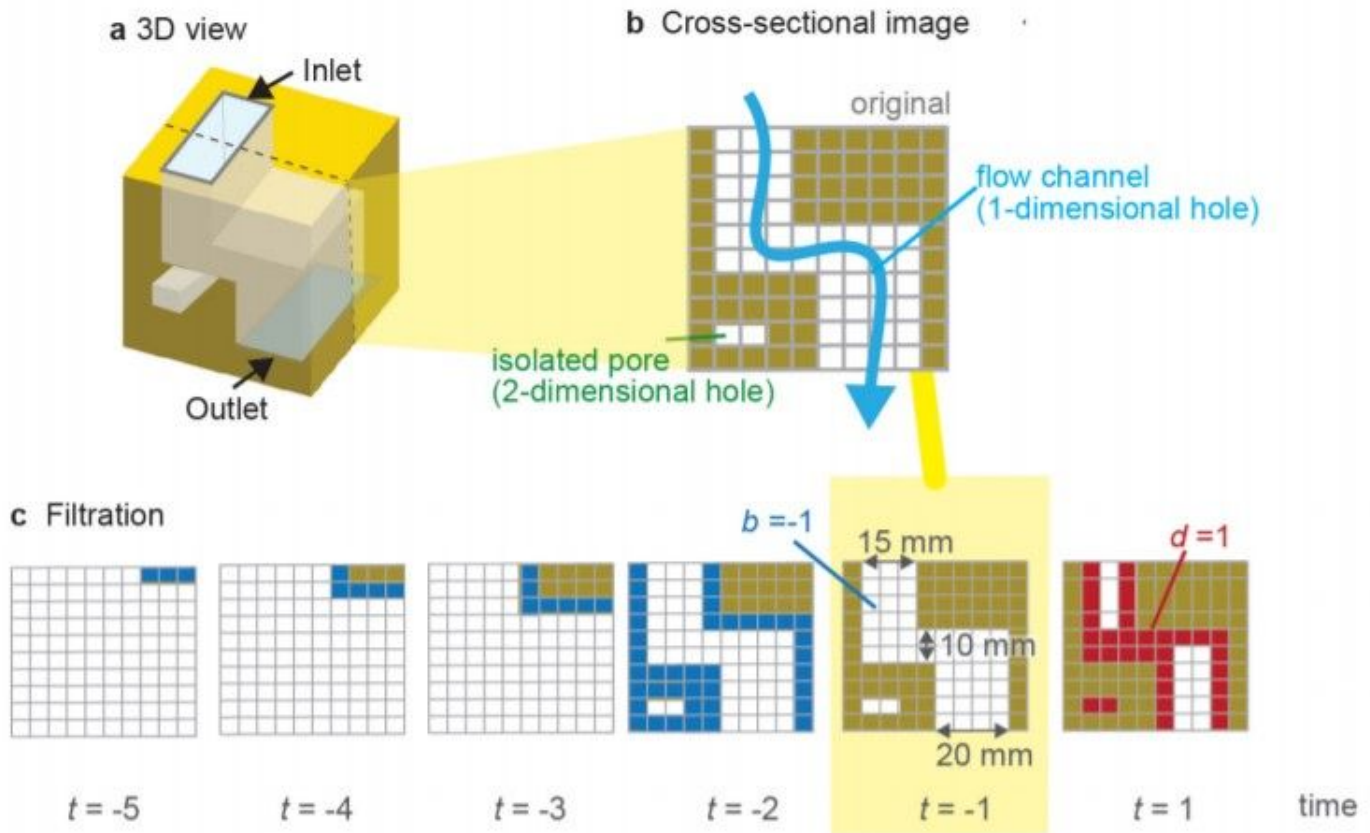


Figure 1

Persistent homology analysis for fracture networks by HomCloud32 . a 3D view and b cross-sectional image of fracture network with a flow channel (light blue arrow) and an isolated pore (mentioned as green). c Schematic of filtration process. Image at $t = -1$ is the original image. White grids express void spaces. Blue grids are the grids that were removed during the thinning process. Red grids are the grids that were added during the thickening process.

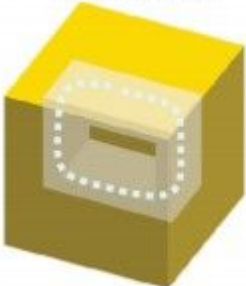
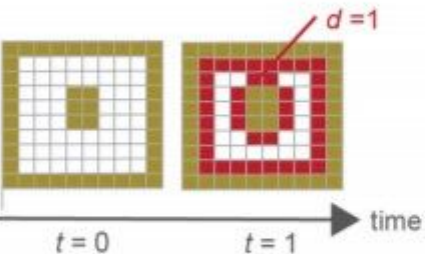
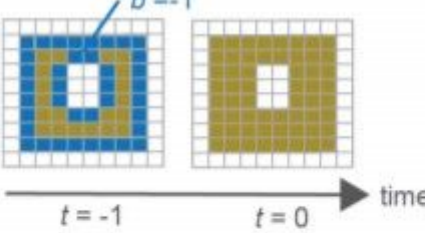
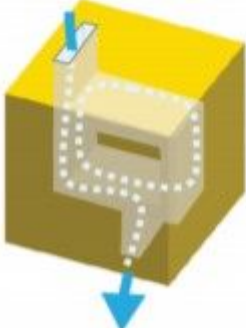
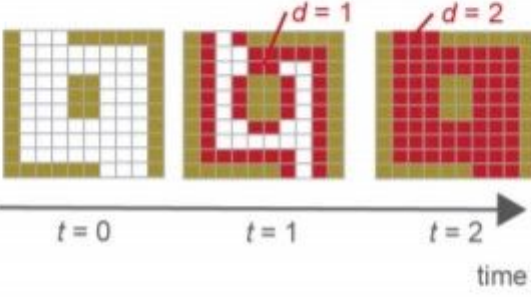
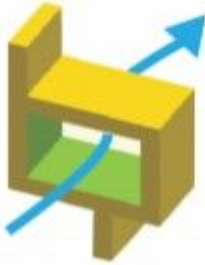
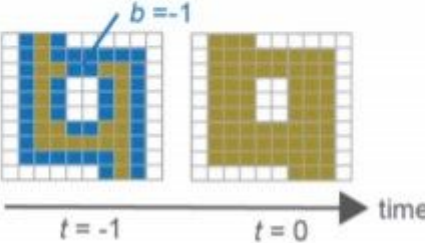
image	filtration	Betti number
a original image 		$\beta_1=1$
b inverted image 		$\bar{\beta}_1=1$
c original image 		$\beta_1=2$
d inverted image 		$\bar{\beta}_1=1$

Figure 2

Detecting flow channels using inverted images a ring-shaped, internal void-structure that is not connected to the outside, and b its inverted image. c ring shaped, internal void-structure with two channels that is connected to the outside and forms a flow channel. d its inverted image. The left column shows 3D view of images. The center column describes processes of filtration. The right column lists Betti numbers β_1 .

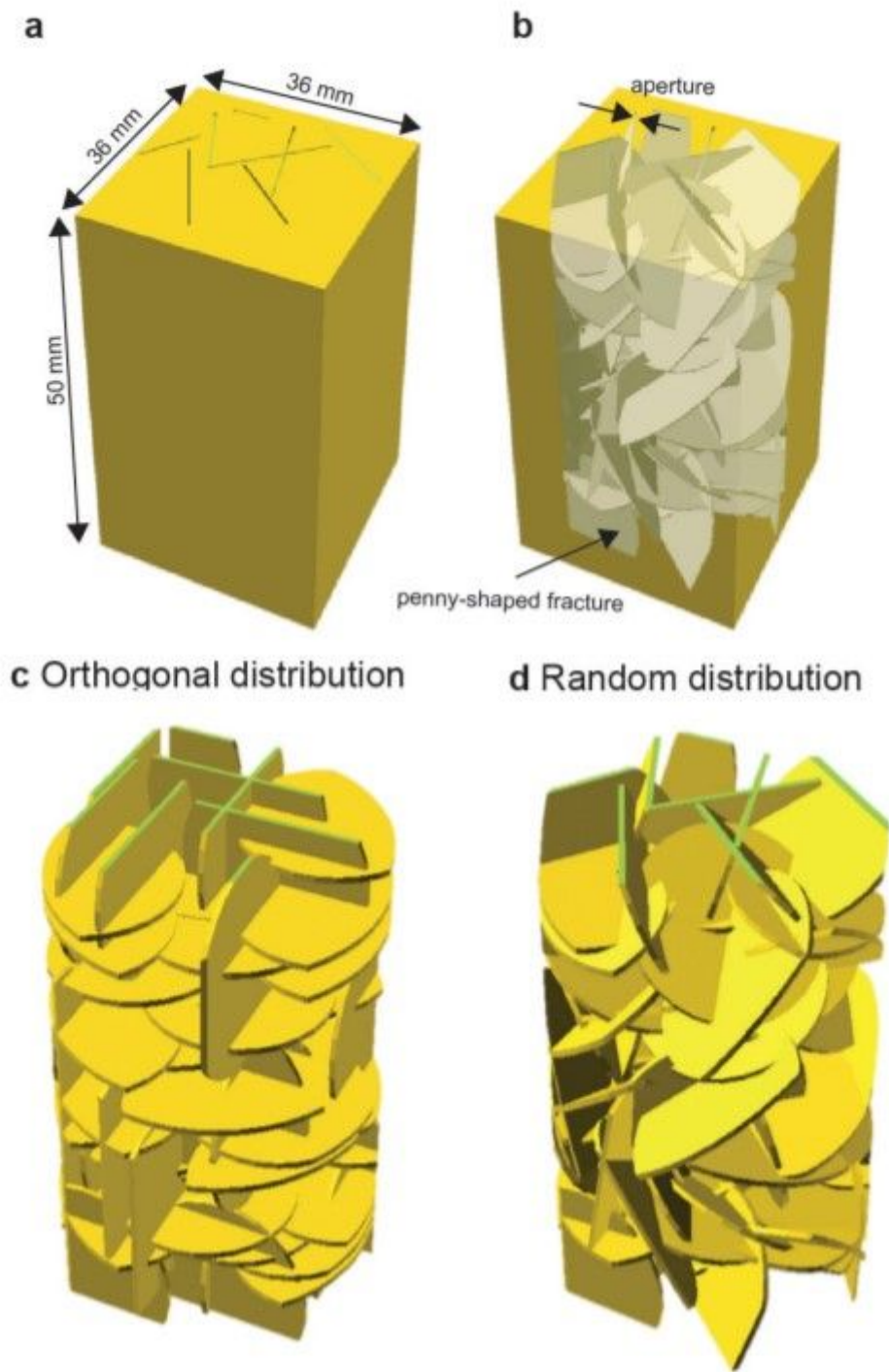


Figure 3

Fractured models. a outside and b inside of model. c Orthogonal distribution and d random distribution of fracture networks.

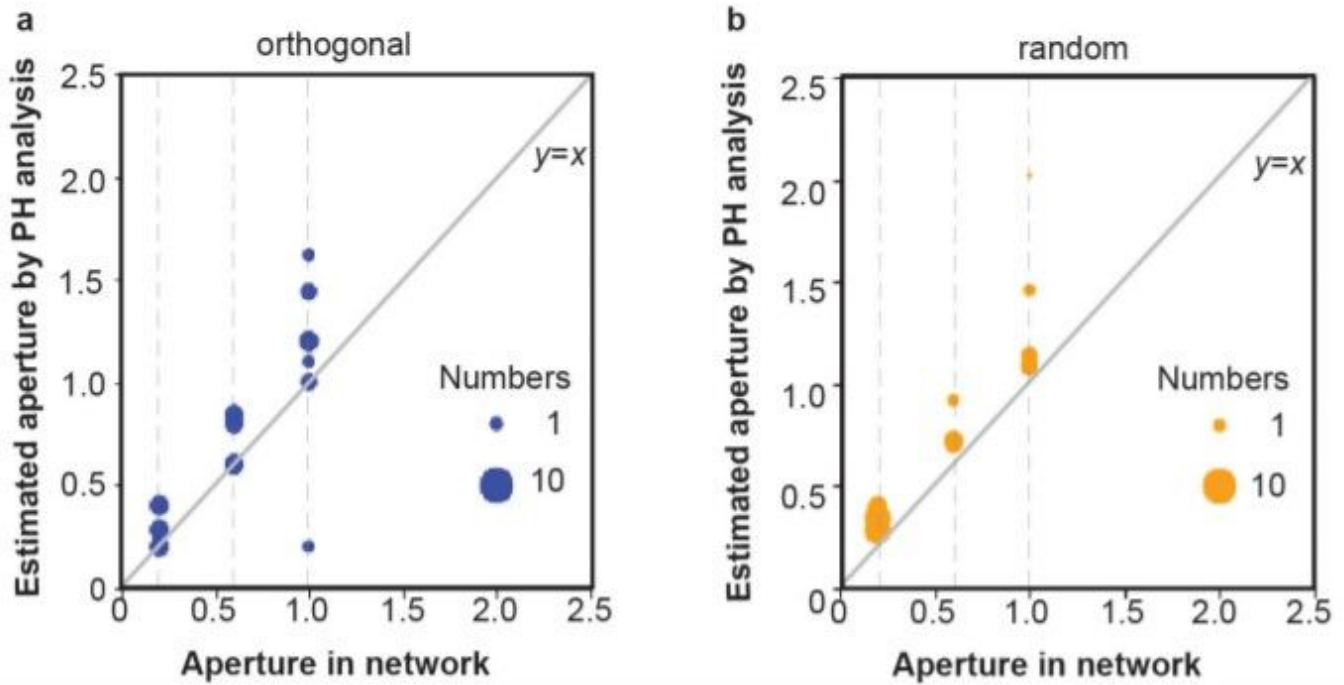


Figure 4

Estimation of fracture apertures by persistent homology (PH) analysis. a orthogonal fracture networks and b random fracture networks.

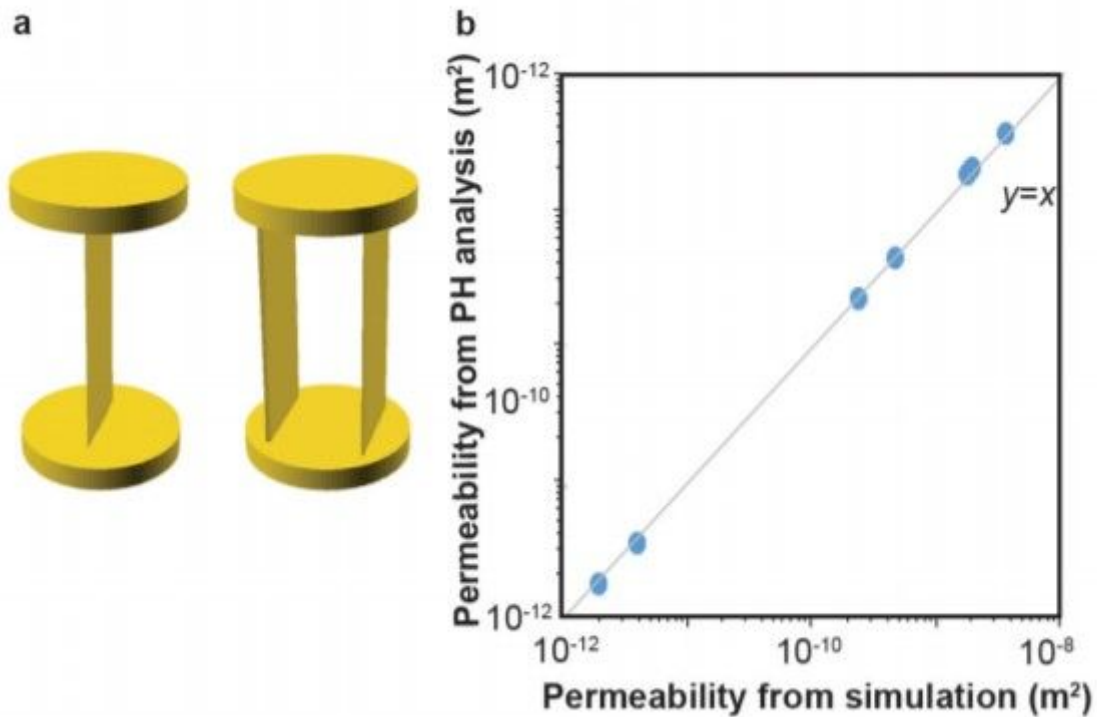


Figure 5

Validation with simple models. a one or two fracture penetrating the model. The top and bottom are the inlet and the outlet. b Comparison of permeability between persistent homology (PH) analysis and direct

simulation. The calculated permeability is listed in Table 2.

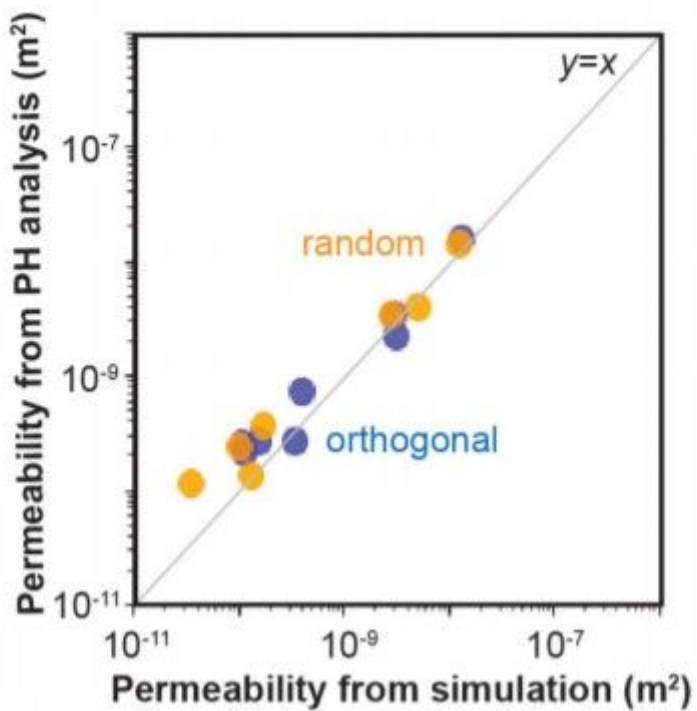


Figure 6

Estimation of permeability by persistent homology (PH) analysis for orthogonal fracture networks (blue) and random fracture networks (orange). The calculated permeability is listed in Table 1.

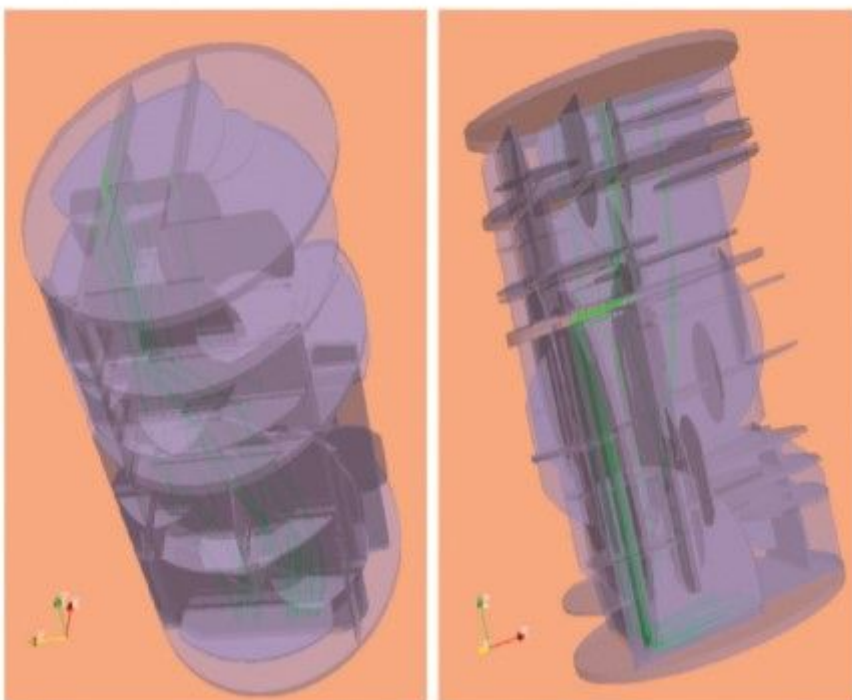


Figure 7

Streamlines (green lines) in fracture network simulated in OpenFOAM

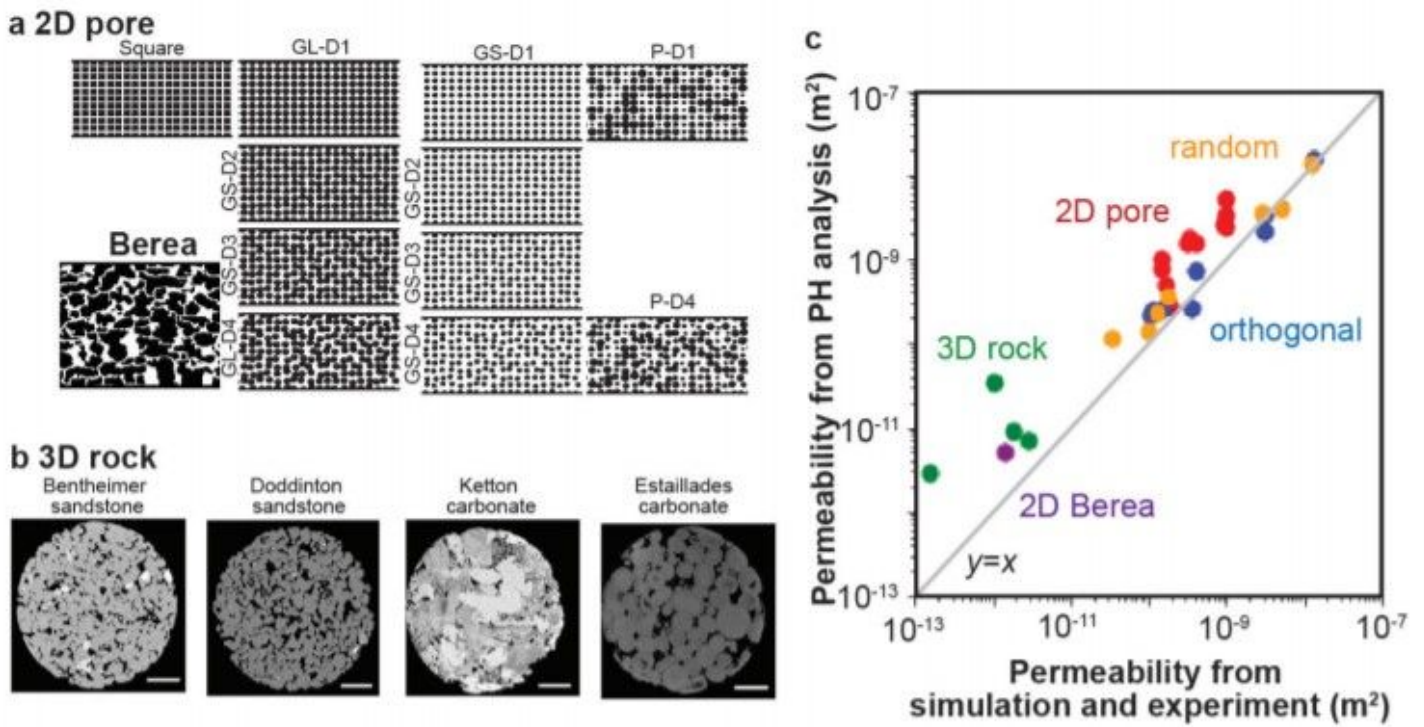


Figure 8

Estimation of permeability by persistent homology (PH) analysis. a 2D images from Mehmani and Hamdi (2015)39, b 3D rock images from Andrew et al. (2014)40, and c comparison with direct simulation and experiment. The values are listed in Table 3.

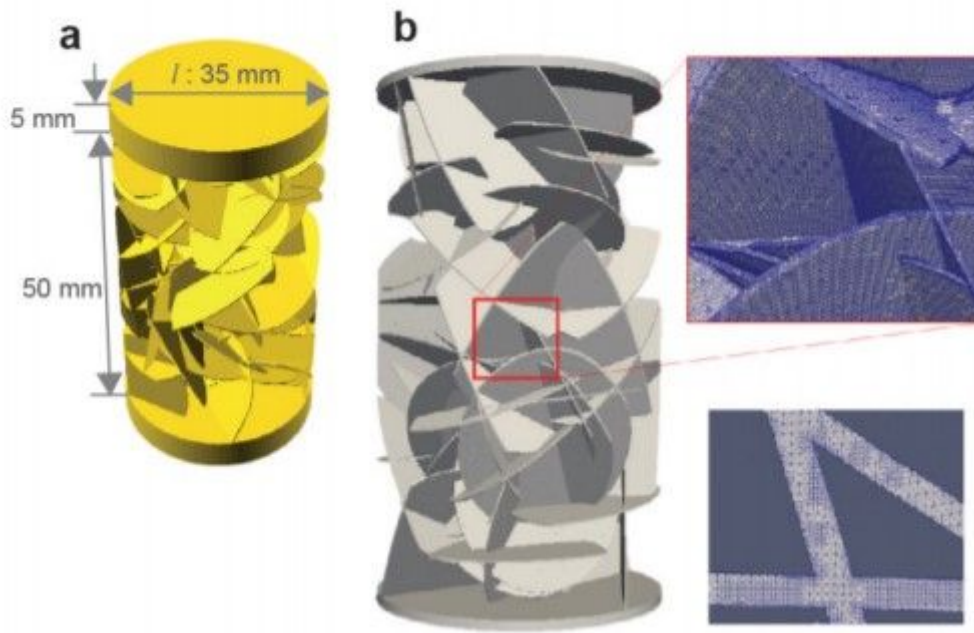


Figure 9

Simulation in OpenFOAM. a fracture network with upper and lower boundaries. b discretized model.